Nanoscale
Advances

PAPER

View Article Online
View Journal | View Issue

Check for updates

Cite this: *Nanoscale Adv.*, 2020, **2**, 3570

Efficient and tunable shape selective synthesis of Ag/CeO$_2$ nanostructures modified highly stable SERS substrate for ultrasensitive detection of pesticides on the surface of an apple

S. Thirumalairajan *[a] and K. Girija [b]

Received 14th May 2020
Accepted 27th June 2020

DOI: 10.1039/d0na00390e

rsc.li/nanoscale-advances

Detection of pesticide residues from fruits and vegetables is of significant importance to ensuring human health and environmental safety. An efficient and tunable shape-selective synthesis of Ag/CeO$_2$ nanostructures as an active flexible SERS substrate for the detection of thiram on an apple surface *via* a paste, peel off, and paste again process was performed. The well-controlled formation of silver assembled CeO$_2$ microspheres constituting nanospheres and nanospindles with an average size of approximately 56 and 32 nm with anisotropic structures has been confirmed through morphological and crystallographic analysis. Interestingly, CeO$_2$ (111) was strongly anchored in the Ag (111) matrix, which provides a more adequate pathway for rapid ion-electron transportation, as observed from the structural and chemical composition analysis. The detection of thiram on the surface of an apple using our proposed nanospindle SERS active substrate achieves a wide detection range from 10^{-2} to 10^{-9} M with a correlation coefficient of 0.9929 and a low detection limit of 27 nM at S/N = 3. In addition, the charge transfer mechanism between the Ag/CeO$_2$ nanostructures and thiram molecules has also been proposed. We believe that the present work could provide novel ways to develop SERS active substrates for highly efficient onsite detection of pesticides on fruits in the near future.

1. Introduction

The detection of pesticide residues in agricultural production has been a crucial problem worldwide, as pesticides are widely used for protecting crops, vegetables, and fruits by regulating insects, and their residues in food could pose a risk, not only to human health but also to the environment and ecology.[1] It has been estimated that less than 0.2% of the pesticide is used to increase the yield and to influence the target pest, and the remaining amount freely enters the environment and may directly contaminate agricultural products and the food chain as reported by the food and nutrient division.[2] India is ranked second in the production of fruits after China, with 24.6% of the world's total production, as indicated by the National Horticultural Board.[3] The intake of pesticide-contaminated fruits and vegetables can cause serious problems to human health even at very low concentrations.[4–6] For instance, thiram is an important pesticide which prevents fungal diseases in seeds, crops, vegetables, and fruits, but is harmful to our skin and this is an important issue with the potential to cause a serious threat.[7,8] Conventional processes such as gas chromatography-mass spectrometry (GC-MS) and high performance liquid chromatography-mass spectrometry (HPLC-MS) for the detection of pesticides on fruits and vegetables are too intricate to be used for monitoring. Also, colorimetric, fluorescent, and electrochemical sensors have been developed as convenient tools for the detection of pesticides. These analytical methods cannot meet the requirements of low detection limit molecular recognition probes and they are time consuming.[9]

Surface-enhanced Raman scattering (SERS) as an effective and sensitive tool, enables the production of an incredibly enhanced Raman signal for the detection of molecules on designed surfaces.[10] SERS shows an enormous enhancement ($\sim 10^8$) of the Raman signal intensity for molecules of interests close to plasmonic (Au or Ag) nanostructures with semiconductor metal oxides.[11–13]

Highly dispersed noble metals (Ag, Au, Pt, Pd, Ru, *etc.*) were used as active components of the semiconductor catalysts and also provide a strong SERS activity. The deposition of Ag over the semiconductor nanostructures is capable of increasing its SERS effect by creating surface plasmon resonance (SPR) and a local dielectric field.[14] CeO$_2$ is a one of the lanthanide series of rare earth metal oxides and has been applied in many applications such as solar cells, sensors, providing oxygen storage capacity, and photoactive and hydrogen production, owing to its redox

---

[a] *Department of Nano Science and Technology, Tamilnadu Agricultural University, Coimbatore-41003, India. E-mail: sthirumalairajan@gmail.com; Fax: +91 422 661 1949; Tel: +91 422 661 1569*

[b] *Department of Physics, Dr N.G.P. Arts and Science College, Coimbatore-641 048, India*

behavior ($Ce^{4+} \leftrightarrow Ce^{3+}$), and it is also environmental friendly, low cost, and has unique physio-chemical properties, hence, CeO_2 is a well-known functional material for SERS studies.[15] Furthermore, significant attention has been paid to the emerging flexible substrate materials in SERS owing to their excellent advantages such as low-cost, easy preparation and being easy to handle.[16–18] Compared with conventional substrates, many flexible materials possess the distinct capacity for intimate contact with real complex surfaces, exhibiting impressive advantages in sampling and rapid analysis with a higher efficiency.[19–23] A very important challenge in the substrate would be to effectively and rapidly collect target molecules from a real complex surface. The majority of SERS substrates are confined to laboratory research and their limitations hinder their practical application.[24–26] Recently, significant efforts have been dedicated to fabricating excellent SERS substrates by controlling the shape, size, and composition of nanostructures that can be applied in scientific and technological applications owing to their large surface area and continuous networks.[27] In addition, the flexible substrates can directly collect targets from complex surfaces with negligible pretreatment through a simple approach, as required. Therefore, SERS detection of pesticide residues in fruits and vegetables in the real world is extremely urgent. To overcome these problems, and also considering the cost evolution, significant attention has been turned towards shape-selective Ag/CeO_2 nanomaterial modified flexible adhesive SERS substrates for the detection of pesticides *via* a paste, peel off and paste again process as an alternative method. However, to the best of our knowledge, shape-selective synthesis of Ag/CeO_2 as flexible SERS active substrates for the detection of pesticide residues on the surface of apples has not been explored in the previously published literature.

In our present work, for the first time, the efficient shape-selective synthesis of an Ag/CeO_2 nanostructure with excellent physicochemical properties for the detection of thiram on the surface of an apple *via* a paste, peel off and paste again process has been discussed. Moreover, the nanostructure, based on CeO_2 and Ag, exhibits synergistic properties. The SERS analysis for the detection of pesticides on apple peels was explored to find the lower limit of detection, sensitivity, anti-interference ability, wide linear range, and good stability. The charge transfer mechanism between the Ag/CeO_2 nanostructures and thiram molecules has also been elucidated. We hope that the developed SERS substrate can be successfully used to regulate the on-site detection of real samples.

2. Experimental section

2.1 Shape selective synthesis of Ag/CeO_2 nanostructures

The Ag/CeO_2 nanostructures were prepared using a facile hydrothermal process using different surfactants as shown in Fig. 1. All chemicals purchased were of an analytical pure grade (Sigma Aldrich) and were used without further purification. In a typical synthetic process, silver nitrate and cerium(III) nitrate hexahydrate were used as the starting materials, and citric acid and sodium dodecyl sulfate (SDS) were used as the structure direct agents. Two different experiments were employed for the synthesis of the Ag/CeO_2 samples. In the first process, cerium(III) nitrate hexahydrate (0.1 M) and the surfactant citric acid (0.1 M) were dissolved in 50 ml of double-distilled water in a stoichiometric ratio of 1 : 1 with vigorous stirring at room temperature for about 30 min. In a separate beaker, 50 ml of 0.1 M silver nitrate solution was mixed with the citric acid solution in a stoichiometric ratio of 1 : 1. Both solutions were

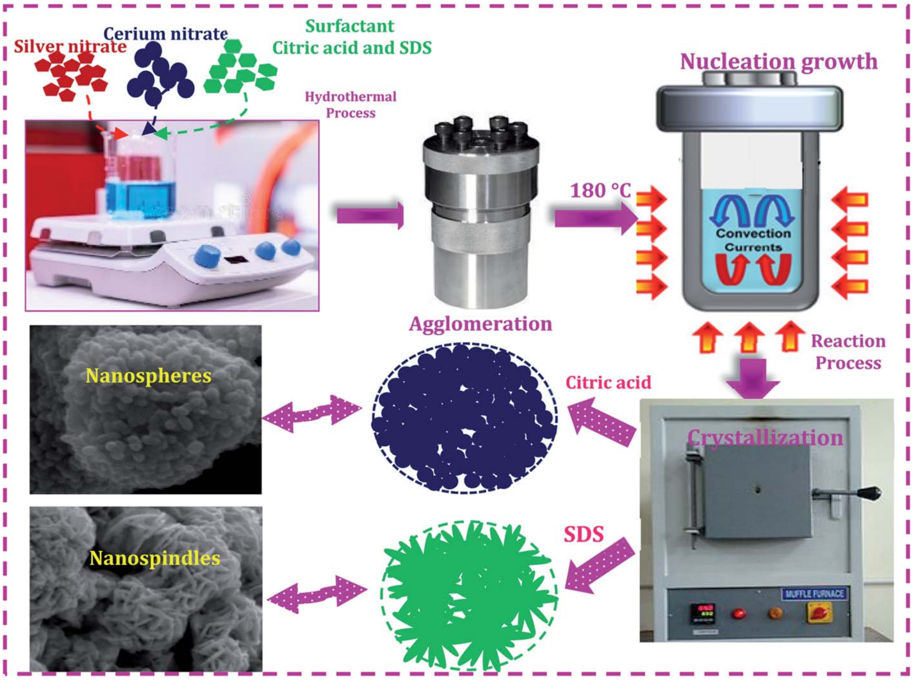

Fig. 1 Schematic illustration of the shape-selective synthesis of the Ag/CeO_2 nanostructures.

mixed and stirred at room temperature until homogeneity was reached. In the second process, citric acid was replaced by SDS, as described in the first experiment, and added to the starting material, resulting in a transparent and homogenous solution. The resulting two solutions were transferred separately into a 110 ml Teflon-lined stainless steel autoclave, sealed and treated at 180 °C overnight. The autoclave was cooled down to room temperature naturally. The obtained materials were separated by centrifugation, washed repeatedly with alcohol and distilled water to remove the unreacted ions, by-products, and organic impurities present in the product, followed by drying at 80 °C and calcination at 600 °C for 2 h to obtain Ag/CeO_2, which was then subjected to characterization techniques.

2.2 Characterization and property analysis

The surface morphology of the prepared samples was investigated using a JEOL JMS-6700F scanning microscope, operating at 3.0 kV. The particle size, elemental mapping, and crystallographic analysis were determined using a transmission electron microscope (TEM, JEOL JEM, Japan) at an accelerating voltage of 200 kV along with the selected area electron diffraction (SAED) pattern. Powder X-ray diffraction (XRD) patterns were collected with a Rigaku X-ray diffraction system equipped with Cu Kα $\lambda = 1.54059$ Å, over a Bragg's angle ranging from 20 to 90°. The spectrum of FT-IR was analyzed within the mid wave number range 4000 to 400 cm^{-1} employing a Thermo Nicolet 200 FTIR spectrometer using the KBr pellet method. The chemical composition and the state of the compositions were surveyed using X-ray photoelectron spectroscopy (XPS, AXIS-NOVA, Kratos, Inc) with an Al Kα (1486.6 eV) irradiation source. The specific surface area and pore volume of the prepared nanostructures were determined using an N_2 adsorption–desorption isotherm Brunauer–Emmett–Teller (BET) analyzer from the Quanta chrome autosorb BET Surface Area. SERS measurements were performed with a Raman spectroscope (LAB Raman HR 800), using a 785 nm laser as an excitation source. The excitation power of the laser was set to 75 mW, and the spectrum collection time was 10 s. All of the SERS spectra results are presented with smoothing and baseline adjustment.

2.3 Fabrication of the SERS substrate

First, the adhesive tape was made immobile on the glass substrate. Then, 10 µl of the 5×10^{-3} M concentration of the shape different Ag/CeO_2 nanostructure solutions were tumbled uniformly onto the sticky side of the tape. The prepared substrate was dried at 30 °C for 2 h, as illustrated in Fig. 2 and used for additional analysis.

2.4 SERS detection of thiram on the surface of an apple

An eating apple was washed with ultrapure water carefully. To fabricate the real sample for SERS analysis, the as-prepared pesticide solution (thiram) was spread onto the apple surface and dried at room temperature. Then, SERS film was pasted onto a particular surface area and pressed. The tape was kept at a certain pressure, pressed for 5 s, and then peeled off carefully and gradually. The SERS film was fixed onto the glass slide for further SERS analysis. To evaluate the SERS performance of our SERS substrate, the enhancement factor (EF) was calculated using the following equation[28]

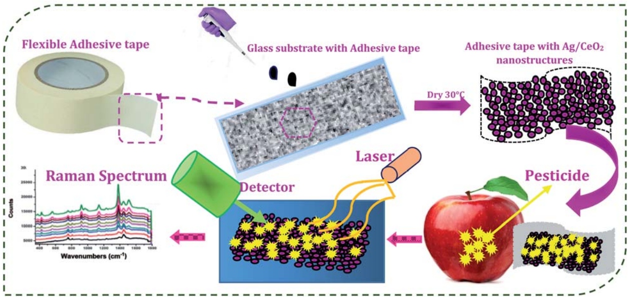

Fig. 2 Schematic illustration of the fabrication of the SERS substrate and detection of the pesticide residues.

$$\mathrm{EF} = [I_{\mathrm{SERS}}/C_{\mathrm{SERS}}]/[I_{\mathrm{Raman}}/C_{\mathrm{Raman}}]$$

In which, C_{Raman} and I_{Raman} are the concentration and peak intensity for the regular Raman measurements with a 10^{-3} M Rh6G solution on a conventionally prepared substrate, whereas C_{SERS} and I_{SERS} are the concentration and peak intensity for the SERS measurement, respectively. The EF of the Ag/CeO_2 nanostructures as a SERS substrate was calculated as 10^8.

3. Results and discussion

3.1 Surface morphological analysis

The surface morphology of the shape-selective synthesis of Ag/CeO_2 nanostructures was achieved by using different structure directing agents, as shown in Fig. 3. Sphere nanostructures were obtained when citric acid was used as the structure-directing agent. The low magnification SEM images of the microsphere with an average diameter of approximately 1.5 µm are shown in Fig. 3a. A detailed understanding of the individual Ag/CeO_2 microspheres can be observed from Fig. 3b and c, which clearly indicates that the individual microspheres consist of many nanospheres with an average size of approximately 50 nm. These nanospheres arise from the single-center, thereby attaining the formation of a microsphere structure *via* a self-assembly process using the hydrothermal process. In addition, when using SDS as a structure directing agent, the microsphere shaped Ag/CeO_2 nanostructures were present as shown in Fig. 3b. This reveals that the individual microspheres have a diameter of approximately 1 µm comprised of small nanospindles in the range of approximately 35 nm as revealed in Fig. 3d.

It can be observed that an individual microsphere is an assembly of many nanospindles, as presented in Fig. 3f. The formation mechanism of both the microspheres can be controlled by intrinsic and extrinsic factors, including the diffusion of the reaction, crystal orientation, surface energy, and the nature of the structure directing agent in the solution reaction system. OH^-

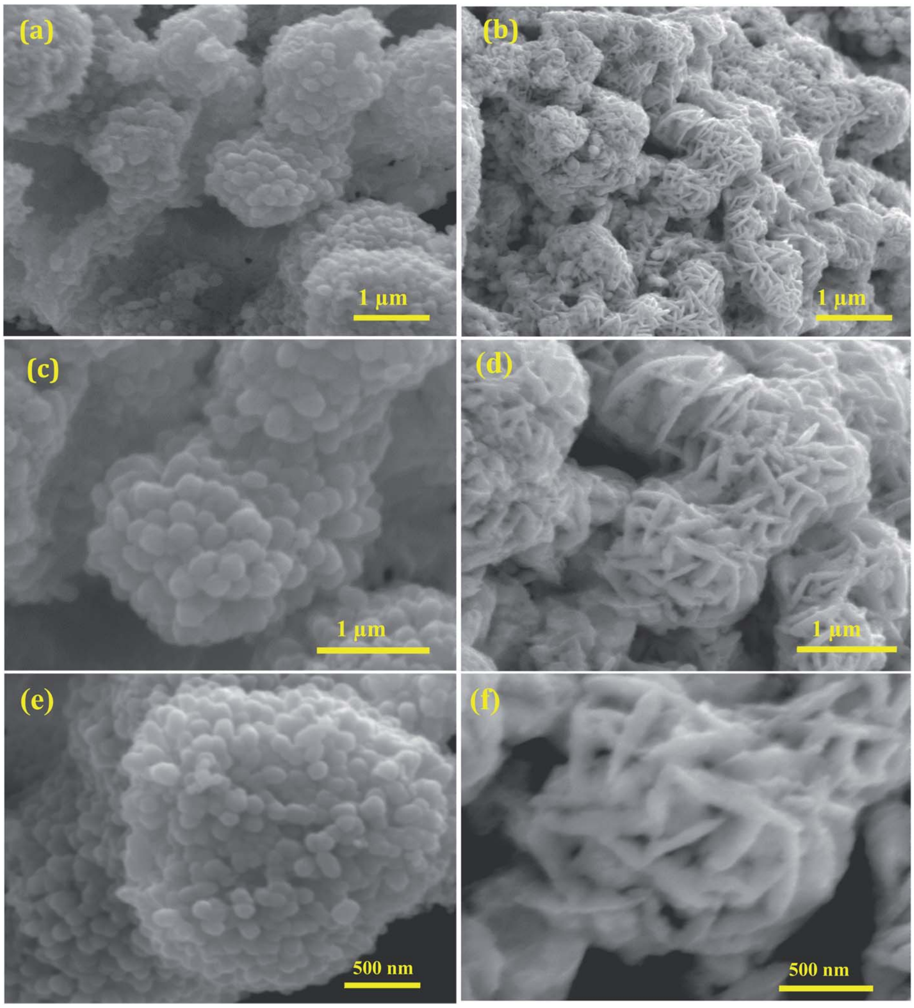

Fig. 3 Low and high magnification SEM images of (a), (c), and (e) microspheres constituting Ag/CeO_2 nanospheres and (b), (d), and (f) microspheres constituting Ag/CeO_2 nanospindles.

ions originating from citric acid and SDS perform a crucial role. When citric acid was used as the structure direct agent, the OH^- ions absorbed on the surface of the Ag/CeO_2 nanospheres directed the self-assembly process of the nanoparticles by molecular interaction to form the microsphere structure with certain crystallographic orientations.[29] When SDS was used as the structure direct agent, the OH^- ions absorbed onto the surface of Ag/CeO_2 were formed in the direction of the reaction process and this continues until the spindles aggregate into microsphere structures *via* nucleation, aggregation, and recrystallization processes. During the reaction process, the structure directing agent is absorbed by the growth rate of the crystal faces, which thereby controls the size and shape through an Ostwald ripening process.[30] Furthermore, Ag/CeO_2 samples without a surfactant were also synthesized, in which only the agglomerated structures were observed, which is of no interest for the present study.

3.2 Particle size and crystallographic analysis

To gain further insights into the shape inside the Ag/CeO_2 microsphere structures, typical TEM, high resolution TEM (HRTEM), and SAED patterns were taken as shown in Fig. 4. The TEM images of the low magnification Ag/CeO_2 microspheres shown in Fig. 4a reveal that the structures have a diameter of approximately 1.5 µm. A part of the microsphere has been investigated using a highly magnified image as shown in Fig. 4c, which shows the presence of numerous Ag/CeO_2 nanospheres with an average size of approximately 50 nm, which is in good agreement with that of the SEM analysis.

Fig. 4b presents the typical TEM image of the formed uniform microsphere structures with an average size of approximately 1 µm, which is composed of a radically assembled spindle structure within the average size of approximately 35 nm (Fig. 4d). From the in-depth observation of the results, it can be reported that the interconnections and formation of the Ag/CeO_2 microspheres are responsible for the nanosphere and nanospindle structures. The HRTEM image recorded at the tip of the individual Ag/CeO_2 nanospheres and nanospindles is presented in Fig. 4e and f. It was observed that the particles are polycrystalline in nature. Also, the interplanar distance was found to be 0.24 and 0.26 nm (Ag), and 0.31 nm (CeO_2) nm

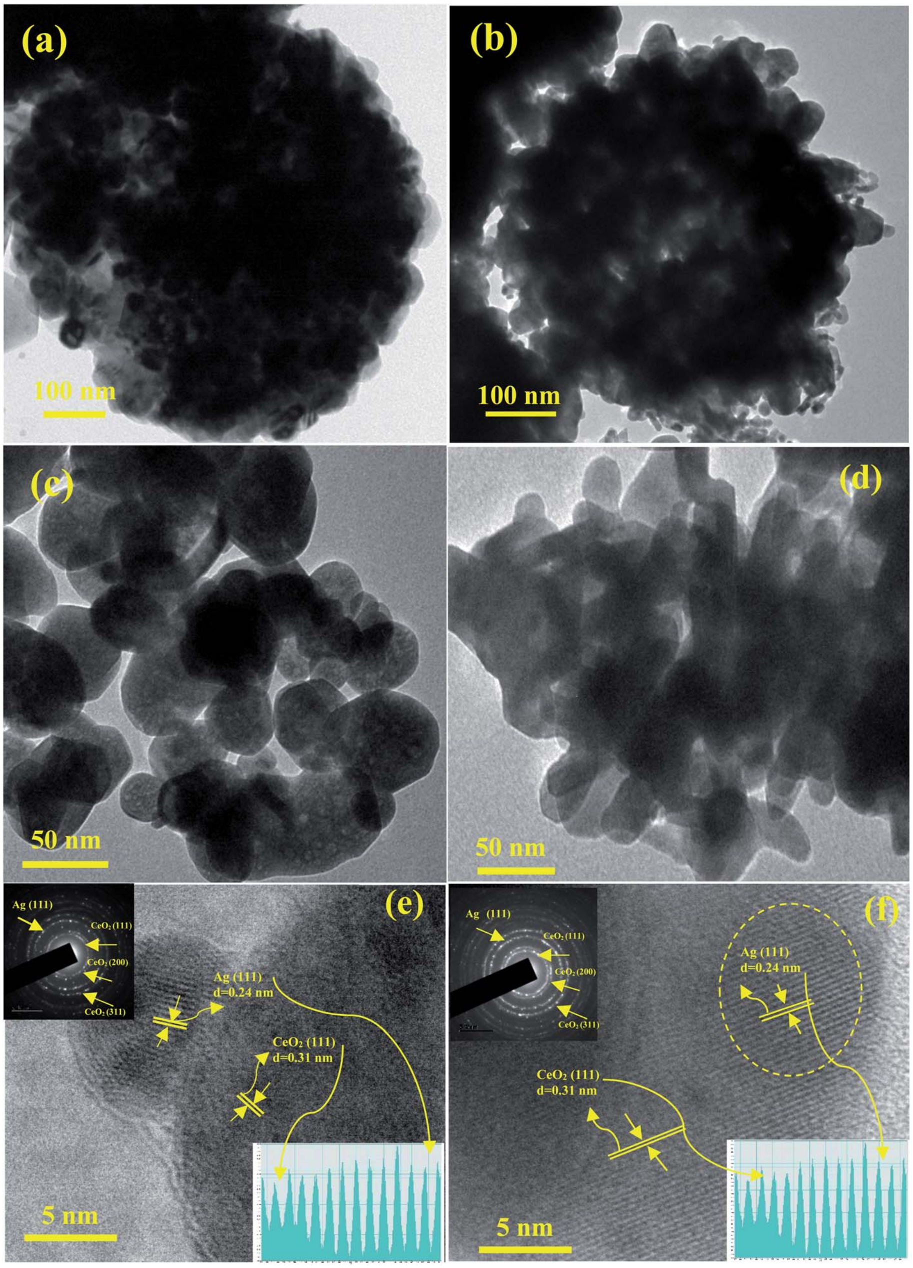

Fig. 4 TEM, HRTEM and SAED pattern images of (a), (c), and (e) nanospheres and (b), (d), and (f) the nanospindles shape of the Ag/CeO_2 nanostructures. The insets in (e) and (f) show the corresponding profile plot for the interlayer spacing (bottom), and the corresponding SAED pattern (top).

based on the measurements of 50 fringes selected at random, as shown in Fig. 4e and f, inset at the bottom. The corresponding lattice interplanar spacing is the lattice plane of Ag (111) and CeO_2 (111) respectively; and in the same direction, further growth of the structure takes place. The SAED pattern of the two different structures has been presented in Fig. 4e and f in the top right corner (inset). The bright diffraction spots can be indexed to the cubic structure of Ag/CeO_2 with a polycrystalline nature. The major diffraction spots correspond to (111) for Ag and (111), (200), and (311) for the CeO_2 planes. No diffraction spots were attributed to impurities or Ag and Ce containing secondary phases. Thus, by correlating the results from the TEM and HRTEM images, it can be concluded that the observed results are in good agreement with the SEM and XRD results.

3.3 Structural analysis

The crystal structure and phase purity of the prepared samples were determined using powder XRD analysis. The XRD patterns of the Ag/CeO_2 nanostructures (spheres and spindles) shown in Fig. 5a, reveal the polycrystalline nature of all the samples and exhibit the mixed phase of the Ag/CeO_2 structures. The observed XRD patterns can be identified and assigned to the cubic fluorite structure of CeO_2 according to JCPDS File no. (34-0394)[31] for

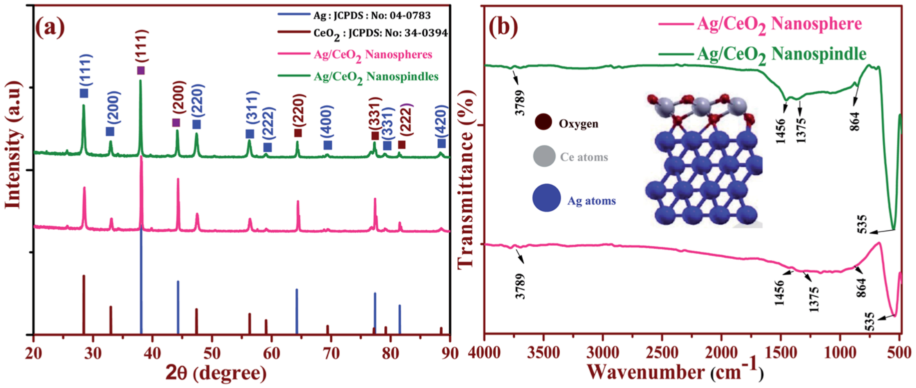

Fig. 5 (a) XRD pattern and (b) FTIR analysis of the shape-dependent Ag/CeO_2 nanostructures.

the diffraction peaks at 2θ values of 28.54, 33.08, 47.48, 56.33, 59.08, 69.4, 76.69 and 79.06° assigned to the (111), (200), (220), (311), (222), (400), (331) and (420) planes, respectively. Similarly, sharp and well-defined peaks indicate that the 2θ values 38.42, 44.35, 64.56 and 81.60° correspond to the (111), (200), (220) and (311) planes assigned to the single face-centered cubic silver (Ag) phase (JCPDS data # 04-0783).[32] No other secondary impurity peaks corresponding to Ag containing or Ce containing phases were detected in the XRD patterns, indicating that the Ag/CeO_2 samples of high purity could be obtained under the preparation conditions. The strong and sharp diffraction peaks suggest that the Ag/CeO_2 nanostructure samples are highly crystalline and the spacing of the lattice fringes were 0.241 nm (Ag) and 0.31 nm (CeO_2), along the growth direction and were well-indexed with the "*d*" spacing of the Ag (111) and CeO_2 (111) plane as discussed in the HRTEM analysis. The average crystallite size calculated using the Debye–Scherrer formula[33] was found to be 51 and 32 nm, respectively. Interestingly, CeO_2 is strongly anchored in the Ag matrix, which provides a more adequate pathway for the charge transfer mechanism which is discussed in a later section.

Furthermore, functional groups were identified using the FTIR spectrum of the shape-dependent Ag/CeO_2 nanostructures recorded in the range of 400 to 4000 cm^{-1} as shown in Fig. 5b. It clearly shows that the absorption band around 3789 cm^{-1} corresponds to the stretching vibration of the –OH functional group. Herein, the bands observed at 1456 cm^{-1} were attributed to the bending vibrations owing to the surface hydroxyl group and the strong band at 1375 cm^{-1} is a result of the Ce–OH stretching vibration. The band at 864 cm^{-1} owing to the stretching mode of the Ce–O bond corresponds to the wavenumber of pure CeO_2 (846 cm^{-1}).[34] The intense peak at 535 cm^{-1} corresponds to the stretching vibration of Ag–O and is found to be a higher wavenumber as compared to 513 cm^{-1} as reported in the literature. This can be attributed to the interaction between the $Ag^{n\delta+}$ nanostructures and oxygen during the redox reaction between Ag and Ce^{3+}, and can also be considered to weaken the Ce–O bond.[35] Additionally, weak absorption peaks can be attributed to the absorption of moisture. These results also agree with the results discussed in the XRD section. Furthermore, for the formation of the interface with Ag, the cerium atoms in the CeO_2 monolayer are all Ce^{4+} cations. After the interface formation, electrons are transferred to CeO_2 from the Ag interface layer. Ag oxidation and electron transfer to ceria were evaluated by calculating the Bader charges on the atoms before and after interface formation.[36] Alignments between the Ag and CeO_2 segments are shown in Fig. 4b (inside), an Ag atom at the interface, a Ce atom of the first CeO_2 is aligned along [111] with the Ag atom, then an O atom of the layer below the Ce layer is aligned with the same Ag atom, and an O atom of the layer above the Ce layer is aligned with the same Ag atom.

3.4 Compositional analysis of shape-dependent Ag/CeO_2 nanostructures

The XPS spectra was examined to identify the chemical composition and the state of the elements for the shape-selective Ag/CeO_2 nanostructures. Fig. 6a displays the survey spectrum of the shape different Ag/CeO_2 nanostructures that exhibit peaks containing Ce 3d, O 1s, Ag 3d, and C 1s that are also consistent with the XRD results. The XPS peak for C 1s is ascribed to the adventitious hydrocarbon from the XPS instrument.

The high resolution spectra of the Ce 3d XPS is shown in Fig. 6b, which reveals the cerium ionic composition, that is Ce^{3+} and Ce^{4+}. The Ce 3d spectrum is composed of two terminals (v and u). These terminals demonstrate the spin–orbit split $3d_{5/2}$ and $3d_{3/2}$ core holes. The spin–orbit splitting is about 18.6 eV. Each spin–orbit component of the Ce 3d XPS spectrum is dominated by three features. Six peaks corresponding to the pairs of spin–orbit doublets can be identified in the Ce $3d_{3/2}$ and Ce $3d_{5/2}$ spectrum, which is in good agreement with other reports.[37] The highest binding energy peaks, u^{iii} and v^{iii}, respectively, located at about 916.79 and 898.46 ± 0.1 eV are the result of the Ce $3d^9 4f^0$ O $2p^6$ final state. The lowest binding energy states u^i, v^i, u^{ii} and v^{ii}, respectively, located at 900.7, 882.1, 907.6, and 888.6 ± 0.1 eV are the result of the Ce $3d^9 4f^2$ O $2p^4$ and Ce $3d^9 4f^1$ O $2p^5$ final states. The existence of the Ce^{4+} and Ce^{3+} states, directly and indirectly, describes the presence of O^- vacancies in the CeO_2 crystals because of their transformations from the Ce^{3+} to Ce^{4+} state.[37] The Ag 3d spectrum of the Ag/CeO_2 sample consisted of two peaks at approximately

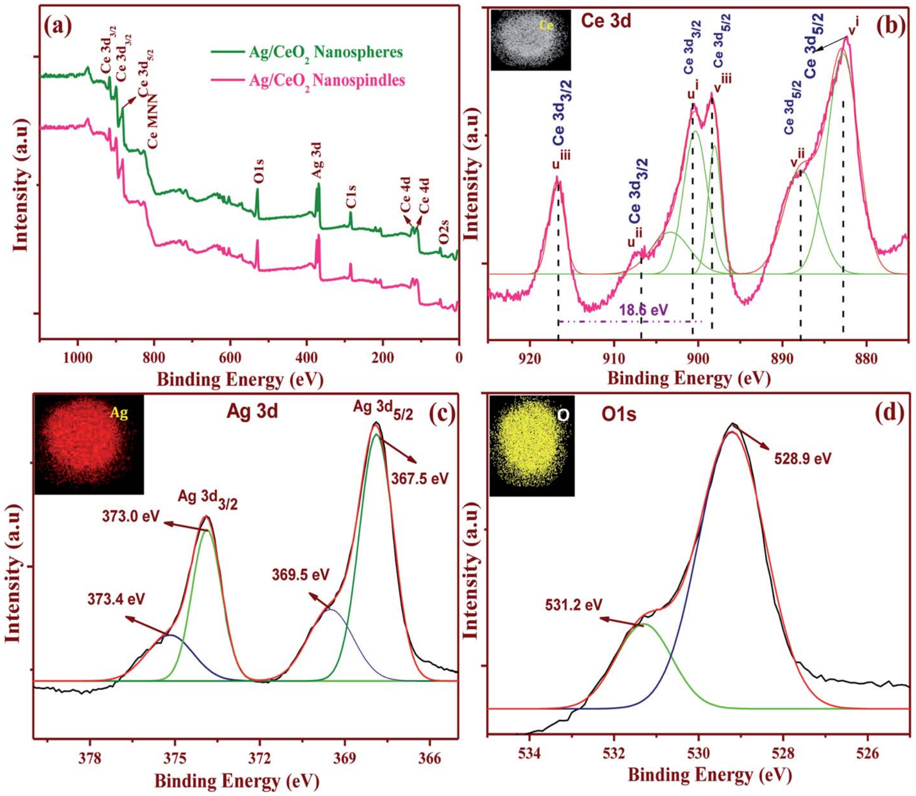

Fig. 6 XPS patterns of the shape-dependent Ag/CeO_2 nanospindles and nanospheres (a) survey spectrum of nanospheres and nanospindles and high-resolution spectra of nanospindles of (b) Ce 3d, (c) Ag 3d and (d) O 1s. The insets show the corresponding elemental mapping.

368 and 374 eV, corresponding to the binding energies of Ag $3d_{5/2}$ and Ag $3d_{3/2}$, as shown in Fig. 6c. These two peaks were further deconvoluted into four peaks at 373.4, 373.0, 367.5, and 369.5 eV. The peaks at 373.4 and 367.5 eV can be attributed to the Ag^{2+} of AgO, whereas the peaks at 373.0 and 369.5 eV can be attributed to the presence of Ag ions over the surface of CeO_2.[38] Fig. 6d revealed that the O 1s XPS consists of two resolved binding energies at 528.9 and 531.2 eV which originate from the O^{2-} confined by the Ce^{4+} ions and O^{2-} ions to the Ce^{3+} ions, respectively. For instance, the elemental mappings of the Ag/CeO_2 nanospheres confirmed the presence of elements such as Ag, Ce, and O as shown in Fig. 6b–d (inset). These clearly demonstrate that the elements were uniformly distributed in the compound. From the relative intensities of the XPS spectra and the elemental mapping, the compositional stoichiometry was calculated between Ag, Ce, and O, and it was found to be about 1 : 1 : 2. This kind of metal–support interaction has been taken as a significant factor in the detection analysis mechanism.

3.5 Surface area analysis of the shape-dependent Ag/CeO_2 nanostructures

The specific surface area and pore volume of the shape-selective synthesis of the Ag/CeO_2 nanostructure samples were studied by using the N_2 adsorption–desorption isotherm

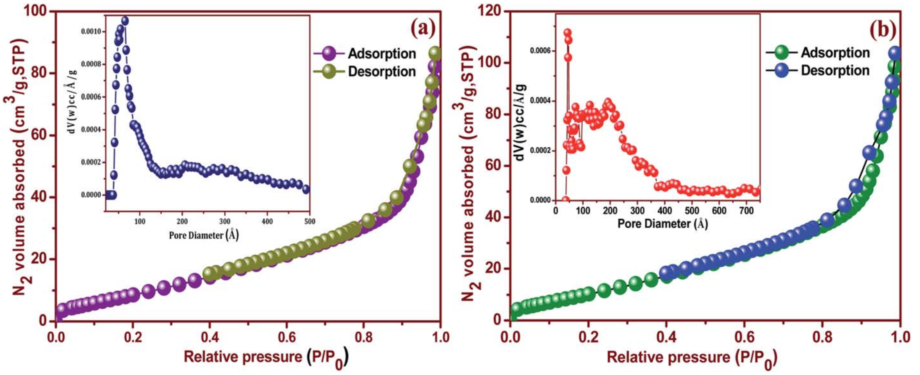

Fig. 7 N_2 adsorption–desorption isotherms of the shape-dependent Ag/CeO_2 nanostructures (a) nanospheres and (b) nanospindles.

using the BET and Barrett–Joyner–Halenda (BJH) methods as shown in Fig. 7a and b. As can be seen in Fig. 7a, the Ag/CeO_2 nanosphere sample exhibits a type-IV isotherm with a hysteresis loop at a relative pressure (P/P_0) of 0.8 to 1. The value of the specific surface area was found to be 87.59 $m^2\ g^{-1}$. Fig. 7a (inset) shows the BJH pore size distribution plot of the Ag/CeO_2 nanospheres, from which the predominant pore volume was found to be 0.516 $cm^3\ g^{-1}$. Meanwhile, the specific surface area and pore volume were measured for the Ag/CeO_2 nanospindles and found to be 135.98 $m^2\ g^{-1}$, and 0.367 $cm^3\ g^{-1}$, by using the corresponding isotherm and distribution profile as shown in Fig. 7b (inset).

The obtained mesoporous characteristics can be ascribed to the presence of an interspace or void in the interconnected packing of both the nanostructure and the large specific surface area when compared to pure CeO_2 (36.85 $m^2\ g^{-1}$).[39] Comparatively, the Ag/CeO_2 nanospindles exhibited a higher specific surface area compared to that obtained for the Ag/CeO_2 nanospheres samples, owing to the size and dimensions formed by aggregation. Thus, both the nanostructures can generate mesoporosity in the material owing to the inter-nanostructure space. The large specific surface area and pore volume indicate that the Ag/CeO_2 nanostructures possess a fascinating ability to adsorb analytes for the detection of pesticides on the surface of fruits, because it is associated to the shape and size.

3.6 Detection of pesticides on the surface of an apple and the possible interaction mechanism

The enhancement factor in SERS is suitable for use in probe molecules that detect pesticides in flexible SERS substrates used for the rapid extraction of trace molecules in fruits and vegetables. Additionally, the sensitivity and stability play a vital role in the flexible SERS-active substrate. We propose a proof-of-concept, SERS active substrate for direct and rapid extraction and detection of the target molecules. From this point of view, thiram appears to be promising for use in testing the Ag/CeO_2 nanostructures. The fungicide is fully insoluble in water but is soluble in nonpolar solvents, thus making it easy to extract from fruits. Furthermore, thiram has a disulfide bond that spontaneously breaks upon exposure to the plasmonic and metal oxide composition substrate. In this work, tunable shape-selective synthesis of an Ag/CeO_2 nanostructures modified flexible adhesive SERS tape substrate was used to detect thiram. 10 μl of the thiram pesticide solution with different concentrations (10^{-2} M to 10^{-9} M) was evenly dropped onto the apple surface and dried at room temperature. Before the detection of pesticides, 10 μl of ethanol was first dropped onto the surface of the peel and then allowed to evaporate naturally. The traces of the thiram were collected from the apple surface using the Ag/CeO_2 nanostructures flexible adhesive substrates *via* a simple "paste and peel off" process. The SERS spectra obtained from the apple surface is shown in Fig. 8a and b. The most intense bands from the detection of thiram using the different Ag/CeO_2 nanosphere

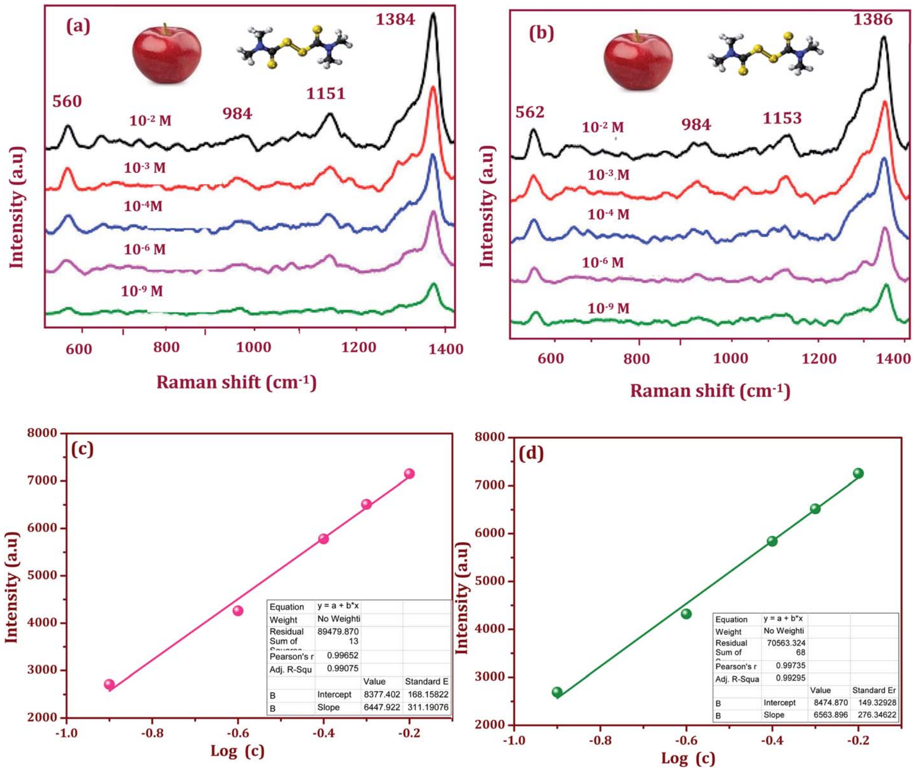

Fig. 8 SERS spectra of thiram on apple peel with different concentrations (10^{-2} to 10^{-9} M) and the linear calibration curves constructed by monitoring the intensity of the strong 1384 and 1386 cm^{-1} spectral feature as a function of the analyte concentration: (a) and (c) Ag/CeO_2 nanospheres, and (b) and (d) Ag/CeO_2 nanospindles.

and nanospindle SERS method were confirmed at 1384 and 1386 cm^{-1} and can be attributed to the CN stretching mode and the symmetric $\delta_s(CH_3)$ deformation mode. As this is the strongest peak in the SERS spectra, the band was used to calibrate the SERS intensity as a function of the thiram concentration. In addition, the peak at 1151 and 1153 cm^{-1} corresponds to both the $\nu_s(CH_3)$ and $\rho(N\cdot CH_3)$ vibrations, the band appearing at 984 cm^{-1} can be assigned to the pure (CN) vibration.[40] The bands at 560 and 562 cm^{-1} can be assigned to ν_s(S–S).[41] The intensity of the major peaks at 1384 and 1386 cm^{-1} depend linearly on the thiram concentration up to 10^{-9} M. Such a significant improvement in the detection sensitivity might be attributed to the higher response of the Ag/CeO_2 nanospindles, as compared with that of the Ag/CeO_2 nanospheres. From these results, our Ag/CeO_2 nanostructures as a SERS substrate revealed a prominent sensitivity to thiram. The reason is the formation of a resonated radical structure to the thiram molecule when interacting with the metal surface, leading to the S–S bond cleavage of thiram, which gives rise to two dimethyl residues that are strongly adsorbed onto the Ag/CeO_2 nanostructures.[42] The experiments with different nanostructures indicate that the Raman signal intensities from the same pesticide behave differently and are distinct. The variations in sensitivity can be attributed to the differences in the surface area, shape, particle size, and SPR performance.

Fig. 8c and d show the linear calibration curve constructed by the shape-selective synthesis of Ag/CeO_2 nanostructures modified flexible adhesive SERS tape substrate as a function of the analyte concentration of thiram. The monitored band at 1384 and 1386 cm^{-1} was chosen as the calibration band owing to its strong intensity. As can been seen, the intensity *versus* log [C] shows an excellent linear relationship. The correlation coefficient R^2 (0.9929) and the limit of detection (LOD) (27 nM) was higher for the Ag/CeO_2 nanospindles, when compared to an $R^2 = 0.9907$ and LOD 30 nM for the Ag/CeO_2 nanospindles. The detection of the thiram molecule proved the feasibility of the prepared SERS substrate for quantitative analysis. The LOD and the correlation coefficient R^2 for each calibration curve was calculated. The limits of quality were calculated and determined by substituting the minimum distinguishable signal to fit the equation of the linear calibration curve.[43]

To evaluate the stability, the Ag/CeO_2 nanostructures modified SERS adhesive substrate was tested under an N_2 atmosphere and ambient environment respectively. As we can see in Fig. 9a and b, for the Ag/CeO_2 nanostructures, the Raman intensity decreased gradually after it was stored for 10 d under ambient conditions, and continued to drop down slowly until the end of the storage day. However, after the 20th day, the Raman intensity did not decrease further and it remained at a high level. This may be attributed to the oxide coating formed rapidly after preparation on the surface of the Ag/CeO_2 nanostructures when exposed to the ambient environment, which in-turn protected the Ag/CeO_2 nanostructures from further oxidation and then remained stable for a longer time.[44] Although the Raman intensity decreased to a certain extent, the intensity did not have a significant impact on the sample detection. Moreover, the Ag/CeO_2 nanostructures modified SERS adhesive substrate exhibits convenient storage in the air without any treatment when compared to the other substrates conserved in water or other organic solvents. Moreover, these modified SERS substrates can retain 98.2% of their initial response after one month of aging effects, which suggests a good long-term stability. The excellent stability of the Ag/CeO_2 nanostructures can be attributed to the unique shape, size, and anti-interference ability.

3.7 Charge transfer mechanism of pesticides and the Ag/CeO_2 nanostructures

Charge transfer mechanisms between the Ag/CeO_2 nanospheres/nanospindles and thiram pesticide molecules are presented in the schematic diagram in Fig. 10. We can observe that, during the interaction between the Ag/CeO_2 nanostructure and the thiram molecule, there is a possibility of a complete charge transfer (CT) system of "donor bridge acceptor" owing to the Fermi level of silver being lower than the surface state energy level of CeO_2.[45] When the Ag particle is in contact with an n-type semiconductor CeO_2, the charge distribution is readjusted for equilibration of the Fermi level between the two particles, which results in the elevation of the Ag Fermi level and the formation of a depletion layer (Schottky barrier) at the junction between the two materials.[46] The Ag assembled in the CeO_2 nanoparticles surface is excited by the incident SERS laser light and the photoexcited electrons are injected into the

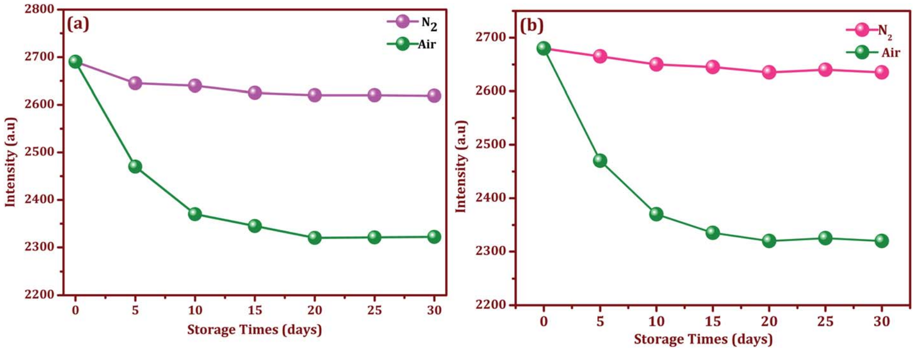

Fig. 9 Stability and storage times for the modified SERS substrate with selected intensities of thiram (10^{-9} M) in an N_2 and air atmosphere: (a) Ag/CeO_2 nanospheres, and (b) Ag/CeO_2 nanospindles.

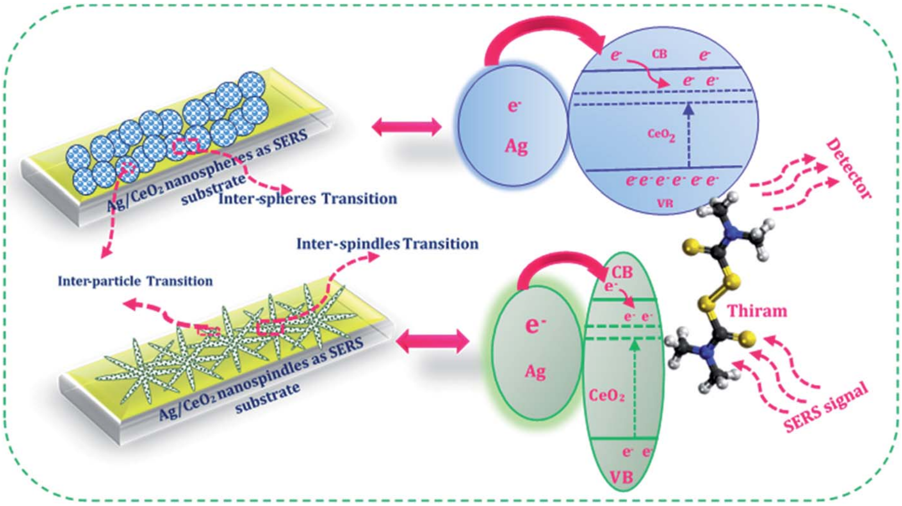

Fig. 10 Schematic illustration of the charge transfer mechanism between the Ag/CeO_2 nanospheres/nanospindles and the pesticide thiram molecules.

conduction band of CeO_2 connected to Ag and/or subsequently onto the lower energy level of CeO_2 and then transferred to the lowest unoccupied molecular orbital (LUMO) energy levels of the molecules adsorbed on the CeO_2 nanoparticles, which enhances the photoabsorption of the charge-transfer complex. These additional electrons provide CeO_2 with a considerable SERS effect for the adsorbed molecules. Also, an intrinsic charge transfer from CeO_2 to thiram and thiram to Ag could occur when the energy levels of the system match the highest occupied molecular orbital (HOMO) and LUMO energy levels of thiram under excitation. Owing to the electromagnetic (generated by Ag particles) and chemical (owing to the charge transfer process) enhancements, the SERS performance of the Ag/CeO_2 nanostructure become enhanced.

The mechanism of the higher SERS enhancement for Ag/CeO_2 nanostructures may be a result of the following reasons. Initially, the SERS enhancement depends on the number of hot spots from the substrates. The hot spots result from narrow junctions between the closely spaced nanoparticles, which are related to the electromagnetic field from the metal nanoparticles. The large SERS enhancement of the probe molecules in Ag/CeO_2 nanostructures can be primarily ascribed to the local electromagnetic effect. A depletion layer may be formed at the interface between the n-type CeO_2 and Ag owing to different work functions.[47] This potential barrier can provide an energetic driving force for exciton dissociation at the interface between CeO_2 and Ag. The formation of band bending at the interface reduces the rate of recombination. This changed the electromagnetic intensity for the Ag/CeO_2 nanostructures, which is the main reason for SERS enhancement. Finally, the Ag/CeO_2 nanostructures revealed a high aspect ratio and an optimally oriented arrangement. The surface area of both the Ag/CeO_2 nanostructures is about five times that of the flat surface of other materials.[48] The high surface area may contact more Ag nanoparticles on the CeO_2 nanospindles/nanospheres. Otherwise, the electron mobility in the CeO_2 nanospheres and nanospindles is larger than that in the particle films owing to their directional and uninterrupted conduction channel.[49–51] This directed transport is expected to increase the electron diffusion constant, thus improving the efficiency of charge collection and enabling the production of incident light. The charge transfer mechanism should help the proposed on-site trace detection of molecules and also revealed that the SERS adhesive substrate has a powerful analytical capability in practical applications.

4. Conclusions

In conclusion, a tunable shape-selective Ag/CeO_2 nanostructure modified SERS adhesive substrate was successfully prepared using a facile wet chemical method and the highly sensitive detection (27 nM) of thiram was explored on the surface of an apple *via* a paste, peel off and paste again process. It is worth emphasizing that the surfactant and reaction temperature leads to the formation of a unique morphology such as nanospheres and nanospindles. The average crystallite size was estimated to be 56 and 32 nm from the XRD, and the lattice fringes were 0.24 and 0.26 nm (Ag) and 0.31 nm (CeO_2) along with the Ag (111) and CeO_2 (111) crystallographic plane of the Ag/CeO_2 nanostructure, which was confirmed from the TEM and HRTEM results. The most important fabricated Ag/CeO_2 nanostructures were of a high specific surface area with more adsorbed oxygen as active sites and exhibited a dynamic wide linear range, a low LOD, good sensitivity and storage stability for thiram detection on the surface of an apple. It is worth emphasizing that the Ag/CeO_2 nanostructures can be implanted within adhesive substrates for sensing with non-planar surfaces in terms of flexible and conformal labels capable of monitoring biological and chemical molecules, as proposed in the charge-transfer interaction mechanism. The reported work demonstrates a feasible strategy to achieve a high performance SERS active substrate for highly efficient onsite detection of pesticides on the surface of an apple in the near future.

Conflicts of interest

The authors declare no conflict of interest related to this work.

Acknowledgements

S. T. gratefully acknowledges financial support from the DBT-Ramalingaswami Re-entry Fellowship scheme 2018–2023, Grant No: D.O.NO:BT/HRD/35/02/2006 dt:19-11-2018 to perform this research.

References

1 E. K. Fodjo, S. Riaz, D. Li, L. L. Qu and N. P. Marius, Cu@Ag/β-AgVO$_3$ as a SERS substrate for the trace level detection of carbamate pesticides, *Anal. Methods*, 2012, **4**(11), 3785–3791.

2 L. K. Chai and F. A. Elie, Rapid multi-residue method for pesticide residues determination in white and black pepper (Piper nigrum L.), *Food Control*, 2013, **32**(1), 322–326.

3 V. Singh, A. N. Patel, A. Dalwadi, J. Kathota, J. Suthar and M. H. Kalubarme, Horticultural Fruit Crop Plantations Mapping using Geo-informatics Technology in Gujarat State India, *International Journal of Advanced Remote Sensing and GIS*, 2017, **6**(2), 2033–2049.

4 Y. Zhang, Z. Wang, L. Wu, Y. Pei, P. Chen and Y. Cui, Rapid simultaneous detection of multi-pesticide residues on apple using SERS technique, *Analyst*, 2014, **139**(20), 5148–5154.

5 S. Dhakal, Y. Li, Y. Peng, K. Chao, J. Qin and L. Guo, Prototype instrument development for non-destructive detection of pesticide residue in apple surface using Raman technology, *J. Food Eng.*, 2014, **123**, 94–103.

6 E. Szpyrka, A. Kurdziel, M. Podbielska and J. Rupar, Evaluation of pesticide residues in fruits and vegetables from the region of south-eastern Poland, *Food Control*, 2015, **48**, 137–142.

7 Z. Zhang, Q. Yu, H. Li, A. Mustapha and M. Lin, Standing gold nanorod arrays as reproducible SERS substrates for measurement of pesticides in apple juice and vegetables, *J. Food Sci.*, 2015, **80**(2), N450–N458.

8 H. Luo, Y. Huang, K. Lai, B. A. Rasco and Y. Fan, Surface-enhanced Raman spectroscopy coupled with gold nanoparticles for rapid detection of phosmet and thiabendazole residues in apples, *Food Control*, 2016, **68**, 229–235.

9 A. B. Nowicka, M. Czaplicka, A. Kowalsa, T. Szymborski and A. Kaminska, Flexible PET/ITO/Ag SERS Platform for Label-Free Detection of Pesticides, *Biosensors*, 2019, **9**(3), 111–118.

10 Z. L. Xu, H. Deng, X. F. Deng, J. Y. Yang and Y. M. Jiang, monitoring of organophosphorus pesticides in vegetables using monoclonal antibody-based direct competitive ELISA followed by HPLC-MS/MS, *Food Chem.*, 2012, **131**(4), 1569–1576.

11 H. Sun, H. Liu and Y. Wu, A green, reusable SERS film with high sensitivity for in-situ detection of thiram in apple juice, *Appl. Surf. Sci.*, 2017, **416**, 704–709.

12 K. Liu, Y. Bai, Z. Yang, Q. Fan and H. Zheng, Porous Au-Ag nanospheres with high-density and highly accessible hotspots for SERS analysis, *Nano Lett.*, 2016, **16**(6), 3675–3681.

13 T. Zhang, Y. Sun, L. Hang, H. Li, G. Liu and Y. Zhang, Periodic porous alloyed Au-Ag nanosphere arrays and their highly sensitive SERS performance with good reproducibility and high density of hotspots, *ACS Appl. Mater. Interfaces*, 2018, **10**(11), 9792–9801.

14 Y. Yang, Q. Zhang, Z. W. Fu and D. Qin, Transformation of Ag nanocubes into Ag-Au hollow nanostructures with enriched Ag contents to improve SERS activity and chemical stability, *ACS Appl. Mater. Interfaces*, 2014, **6**(5), 3750–3757.

15 W. Li, R. Zamani, P. Rivera Gil, B. Pelaz, M. Ibáñez, A. Cadavid and A. Cabot, CuTe nanocrystals: shape and size control, plasmonic properties, and use as SERS probes and photothermal agents, *J. Am. Chem. Soc.*, 2013, **135**(19), 7098–7101.

16 G. Lu, T. Forbes and A. J. Haes, SERS detection of uranyl using functionalized gold nanostars promoted by nanoparticle shape and size, *Analyst*, 2016, **141**(17), 5137–5143.

17 R. Boyack and E. C. Le Ru, Investigation of particle shape and size effects in SERS using T-matrix calculations, *Phys. Chem. Chem. Phys.*, 2009, **11**(34), 7398–7405.

18 C. Caro, P. Quaresma, E. Pereira, J. Franco, M. Pernia Leal, D. García-Martín and D. Pozo, Synthesis and characterization of elongated-shaped silver nanoparticles as a biocompatible anisotropic SERS probe for intracellular imaging: theoretical modeling and experimental verification, *Nanomaterials*, 2019, **9**(2), 256.

19 H. Kang, C. J. Heo, H. C. Jeon, S. Y. Lee and S. M. Yang, Durable plasmonic cap arrays on flexible substrate with real-time optical tunability for high-fidelity SERS devices, *ACS Appl. Mater. Interfaces*, 2013, **5**(11), 4569–4574.

20 D. Cheng, M. He, J. Ran, G. Cai, J. Wu and X. Wang, Depositing a flexible substrate of triangular silver nanoplates onto cotton fabrics for sensitive SERS detection, *Sens. Actuators, B*, 2018, **270**, 508–517.

21 A. J. Chung, Y. S. Huh and D. Erickson, Large area flexible SERS active substrates using engineered nanostructures, *Nanoscale*, 2011, **3**(7), 2903–2908.

22 S. K. Bhunia, L. Zeiri, J. Manna, S. Nandi and R. Jelinek, Carbon-dot/silver-nanoparticle flexible SERS-active films, *ACS Appl. Mater. Interfaces*, 2016, **8**(38), 25637–25643.

23 H. Wu, Y. Luo, C. Hou, D. Huo, Y. Zhou and Y. Lei, Flexible bipyramid-AuNPs based SERS tape sensing strategy for detecting methyl parathion on vegetable and fruit surface, *Sens. Actuators, B*, 2019, **285**, 123–128.

24 J. Jiang, S. Zou, Y. Li, F. Zhao, J. Chen, Z. Wang and Z. Zhang, Flexible and adhesive tape decorated with silver nanorods for in-situ analysis of pesticides residues and colorants, *Microchim. Acta*, 2019, **186**(9), 603–611.

25 J. Jiang, S. Zou, L. Ma, S. Wang, J. Liao and Z. Zhang, Surface-enhanced Raman scattering detection of pesticide residues using transparent adhesive tapes and coated silver nanorods, *ACS Appl. Mater. Interfaces*, 2018, **10**(10), 9129–9135.

26 K. Xu, R. Zhou, K. Takei and M. Hong, Toward Flexible Surface-Enhanced Raman Scattering Sensors for Point-of-Care Diagnostics, *Adv. Sci.*, 2019, **6**(16), 1900925.

27 J. Xie, L. Li, I. M. Khan, Z. Wang and X. Ma, Flexible paper-based SERS substrate strategy for rapid detection of methyl parathion on the surface of fruit, *Spectrochim. Acta, Part A*, 2020, **231**, 118104.

28 Z. Li, X. Huang and G. Lu, Recent developments of flexible and transparent SERS substrates, *J. Mater. Chem. C*, 2020, **8**(12), 3956–3969.

29 C. Yuan, R. Liu, S. Wang, G. Han, M. Y. Han, C. Jiang and Z. Zhang, Single clusters of self-assembled silver nanoparticles for surface-enhanced Raman scattering sensing of a dithiocarbamate fungicide, *J. Mater. Chem.*, 2011, **21**(40), 16264–16270.

30 Z. Li, X. Huang and G. Lu, Recent developments of flexible and transparent SERS substrates, *J. Mater. Chem. C*, 2020, **8**(12), 3956–3969.

31 S. Thirumalairajan, V. R. Mastelaro and C. A. Escanhoela Jr, In-depth understanding of the relation between $CuAlO_2$ particle size and morphology for ozone gas sensor detection at a nanoscale level, *ACS Appl. Mater. Interfaces*, 2014, **6**(23), 21739–21749.

32 S. Thirumalairajan, K. Girija, V. Ganesh, D. Mangalaraj and N. Ponpandian, Novel synthesis of $LaFeO_3$ nanostructure dendrites: a systematic investigation of growth mechanism, properties, and biosensing for highly selective determination of neurotransmitter compounds, *Cryst. Growth Des.*, 2013, **13**(1), 291–302.

33 S. A. Mock, S. E. Sharp, T. R. Stoner, M. J. Radetic, E. T. Zell and R. Wang, CeO_2 nanorods-supported transition metal catalysts for CO oxidation, *J. Colloid Interface Sci.*, 2016, **466**, 261–267.

34 T. Sinha and M. Ahmaruzzaman, High-value utilization of egg shell to synthesize silver and gold-silver core shell nanoparticles and their application for the degradation of hazardous dyes from aqueous phase-A green approach, *J. Colloid Interface Sci.*, 2015, **453**, 115–131.

35 U. Holzwarth and N. Gibson, The Scherrer equation versus the 'Debye-Scherrer equation', *Nat. Nanotechnol.*, 2011, **6**(9), 534.

36 F. Lu, B. Jiang, J. Wang, Z. Huang, Z. Liao, Y. Yang and J. Zheng, Promotional effect of Ti doping on the ketonization of acetic acid over a CeO_2 catalyst, *RSC Adv.*, 2017, 7(36), 22017–22026.

37 F. Yang, J. Huang, T. Odoom-Wubah, Y. Hong, M. Du and Q. Li. Sun, Efficient Ag/CeO_2 catalysts for CO oxidation prepared with microwave assisted biosynthesis, *Chem. Eng. J.*, 2015, **269**, 105–112.

38 Z. Qu, F. Yu, X. Zhang, Y. Wang and J. Gao, Support effects on the structure and catalytic activity of mesoporous Ag/CeO_2 catalysts for CO oxidation, *Chem. Eng. J.*, 2013, **229**, 522–532.

39 M. L. Rocha, G. Del Ángel, G. Torres-Torres, A. Cervantes, A. Vázquez, A. Arrieta and J. N. Beltramini, Effect of the Pt oxidation state and Ce^{3+}/Ce^{4+} ratio on the Pt/TiO_2-CeO_2 catalysts in the phenol degradation by catalytic wet air oxidation (CWAO), *Catal. Today*, 2015, **250**, 145–154.

40 L. Wu, S. Fang, L. Ge, C. Han, P. Qiu and Y. Xin, Facile synthesis of Ag@CeO_2 core-shell plasmonic photocatalysts with enhanced visible-light photocatalytic performance, *J. Hazard. Mater.*, 2015, **300**, 93–103.

41 K. Saravanakumar, M. Ramjan, P. Suresh and V. Muthuraj, Fabrication of highly efficient visible-light-driven Ag/CeO_2 photocatalyst for degradation of organic pollutants, *J. Alloys Compd.*, 2016, **664**, 149–160.

42 A. M. Fales and T. Vo-Dinh, Silver embedded nanostars for SERS with internal reference (SENSIR), *J. Mater. Chem. C*, 2015, 3(28), 7319–7324.

43 S. Pang, T. Yang and L. He, Review of surface enhanced Raman spectroscopic detection of synthetic chemical pesticides, *TrAC, Trends Anal. Chem.*, 2016, **85**, 73–82.

44 Y. Zhu, M. Li, D. Yu and L. Yang, A novel paper ragas 'D-SERS' substrate for detection of pesticide residues at various peels, *Talanta*, 2014, **128**, 117–124.

45 P. Guo, D. Sikdar, X. Huang, K. J. Si, W. Xiong, S. Gong and W. Cheng, Plasmonic core-shell nanoparticles for SERS detection of the pesticide thiram: size-and shape-dependent Raman enhancement, *Nanoscale*, 2015, **7**(7), 2862–2868.

46 T. Yaseen, H. Pu and D. W. Sun, Fabrication of silver-coated gold nanoparticles to simultaneously detect multi-class insecticide residues in peach with SERS technique, *Talanta*, 2019, **196**, 537–545.

47 Y. Kang, L. Li, W. Chen, F. Zhang, Y. Du and T. Wu, Rapid In Situ SERS Analysis of Pesticide Residues on Plant Surfaces Based on Micelle Extraction of Targets and Stabilization of Ag Nanoparticle Aggregates, *Food Anal. Methods*, 2018, **11**(11), 3161–3169.

48 L. Ren, X. Xian, K. Yan, L. Fu, Y. Liu, S. Chen and Z. Liu, A General Electrochemical Strategy for Synthesizing Charge-Transfer Complex Micro/Nanowires, *Adv. Funct. Mater.*, 2010, **20**(8), 1209–1223.

49 K. K. Chin, S. H. Pan, D. Mo, P. Mahowald and N. Newman, Electronic structure and Schottky-barrier formation of Ag on n-type GaAs (110), *Phys. Rev. B: Condens. Matter Mater. Phys.*, 1985, **32**(2), 918.

50 X. J. Wen, C. G. Niu, L. Zhang, C. Liang and H. Guo, Photocatalytic degradation of ciprofloxacin by novel Z-scheme CeO_2-Ag/AgBr photocatalyst: influencing factors, possible degradation pathways, and mechanism insight, *J. Catal.*, 2018, **358**, 141–154.

51 N. Sasirekha, P. Sangeetha and Y. W. Chen, Bimetallic Au-Ag/CeO_2 catalysts for preferential oxidation of CO in hydrogen-rich stream: effect of calcination temperature, *J. Phys. Chem. C*, 2014, **118**(28), 15226–15233.